JLAB USER GROUP

Jefferson Lab PAC13
Proposal Cover Sheet

This document must be received by close of business Thursday, December 18, 1997 at:

Jefferson Lab
User Liaison Office,
Mail Stop 12B
12000 Jefferson Avenue
Newport News, VA
23606

Experimental Hall: C

Days Requested for Approval: 0 Additional*

*Run concurrent with G0 backward angle measurement.

☒ New Proposal Title: Measurement of the Parity Violating Asymmetry in the N to Delta Transition.

☐ Update Experiment Number:

☐ Letter-of-Intent Title:

(Choose one)

Proposal Physics Goals

Indicate any experiments that have physics goals similar to those in your proposal.

Approved, Conditionally Approved, and/or Deferred Experiment(s) or proposals:

E94-005

Contact Person

Name: S.P. Wells, N. Simicevic, K. Johnston

Institution: LOUISIANA TECH UNIVERSITY

Address: Dept. of Physics

Address: P.O.Box 3169 T.S.

City, State, ZIP/Country: Ruston, LA 71272, USA

Phone: (318)257-2194 Fax: (318)257-4228

E-Mail: wells@phys.latech.edu, simicevic@phys.latech.edu, johnston@phys.latech.edu

JLab Use Only

Receipt Date: 12/18/97 PR-97-104

By: gp

BEAM REQUIREMENTS LIST

Lab Proposal No.: _____ Date: _____

Hall: C Anticipated Run Date: 2000 PAC Approved Days: _____

Spokesperson: S.P.Wells, N.Simicevic, K.Johnston Hall Liaison: Roger Carlini
Phone: (318) 257-2194
E-mail: wells@phys.latech.edu
Simicevic@phys.latech.edu
johnston@ phys.latech.edu

List all combinations of anticipated targets and beam conditions required to execute the experiment. (This list will form the primary basis for the Radiation Safety Assesment Document (RSAD) calculations that must be performed for each experiment.)

Condition No.	Beam Energy (MeV)	Mean Beam Current (μA)	Polarization and Other Special Requirements (e.g., time structure)	Target Material (use multiple rows for complex targets — e.g., w/windows)	Material Thickness (mg/cm²)	Est. Beam-On Time for Cond. No. (hours)
1	933	40	70%, 31.25 MHz	LH_2	0.7	700*
2	659	40	70%, 31.25 MHz	LH_2	1.4	700*
3	585	40	70%, 31.25 MHz	LH_2	1.4	700*
4	507	40	70%, 31.25 MHz	LH_2	1.4	700*
5	424	40	70%, 31.25 MHz	LH_2	1.4	700*

*All running concurrent with G0 backward angle measurements.

The beam energies, E_{Beam}, available are: $E_{Beam} = N \times E_{Linac}$ where N = 1, 2, 3, 4, or 5. E_{Linac} = 800 MeV, i.e., available E_{Beam} are 800, 1600, 2400, 3200, and 4000 MeV. Other energies should be arranged with the Hall Leader before listing.

HAZARD IDENTIFICATION CHECKLIST

JLab Proposal No.: _____ Date: _____
(For CEBAF User Liaison Office use only.)

Check all items for which there is an anticipated need.

Cryogenics _____ beamline magnets _____ analysis magnets _____ target type: LH_2 flow rate: 333 g/s capacity: 6.6 l	**Electrical Equipment** _____ cryo/electrical devices _____ capacitor banks _____ high voltage _____ exposed equipment	**Radioactive/Hazardous Materials** List any radioactive or hazadorous/ toxic materials planned for use: _____ _____ _____ _____
Pressure Vessels _____ inside diameter _____ operating pressure _____ window material _____ window thickness	**Flammable Gas or Liquids** type: _____ flow rate: _____ capacity: _____ **Drift Chambers** type: _____ flow rate: _____ capacity: _____	**Other Target Materials** ___ Beryllium (Be) ___ Lithium (Li) ___ Mercury (Hg) ___ Lead (Pb) ___ Tungsten (W) ___ Uranium (U) ___ Other (list below) _____ _____
Vacuum Vessels _____ inside diameter _____ operating pressure _____ window material _____ window thickness	**Radioactive Sources** _____ permanent installation _____ temporary use type: _____ strength: _____	**Large Mech. Structure/System** _____ lifting devices _____ motion controllers _____ scaffolding or _____ elevated platforms
Lasers type: _____ wattage: _____ class: _____ Installation: _____ permanent _____ temporary Use: _____ calibration _____ alignment	**Hazardous Materials** ____ cyanide plating materials ____ scintillation oil (from) ____ PCBs ____ methane ____ TMAE ____ TEA ____ photographic developers ____ other (list below) _____ _____	**General:** Experiment Class: _____ Base Equipment _____ Temp. Mod. to Base Equip. _____ Permanent Mod. to Base Equipment _____ Major New Apparatus Other: _____ _____

LAB RESOURCES LIST

JLab Proposal No.: _____ Date _____
(For JLab ULO use only.)

List below significant resources — both equipment and human — that you are requesting from Jefferson Lab in support of mounting and executing the proposed experiment. Do not include items that will be routinely supplied to all running experiments such as the base equipment for the hall and technical support for routine operation, installation, and maintenance.

Major Installations *(either your equip. or new equip. requested from JLab)*

1) Rotate GO Sprectometer 180°

2) Install CED's

New Support Structures:

Data Acquisition/Reduction

Computing Resources:

New Software:

Major Equipment

Magnets:

Power Supplies:

Targets:

Detectors: CED's

Electronics:

Computer Hardware:

Other:

Other:

Measurement of the Parity Violating Asymmetry in the $N \rightarrow \Delta$ Transition

S.P. Wells, N. Simicevic, and K. Johnston
Center for Applied Physics Studies
Louisiana Tech University
Ruston, Louisiana 71272
and
The G0 Collaboration

Abstract

We propose to make measurements of the parity violating asymmetry in inclusive pion electroproduction from the proton through the region of the Δ resonance in the Q^2 range $0.05 \leq Q^2 \leq 0.8$ (GeV/c)^2. These measurements will be made using the G0 spectrometer in its backward angle mode during the same running period as the elastic $\vec{e}+p$ parity violating asymmetry measurements. The large acceptance of the G0 spectrometer presents the unique opportunity of mapping the Q^2 dependence of the asymmetry across the Δ resonance and the parity violating asymmetry for elastic $\vec{e}+p$ scattering simultaneously. At the same time as the G0 elastic measurements will be made, we will achieve a statistical precision of $\sim 3\%$ for the inelastic asymmetry in each of the Q^2 bins measured for the reaction. In the low energy regime, and at backward electron scattering angles, where these measurements will be made, the parity violating asymmetry in the inelastic channel has enhanced sensitivity to the $N \rightarrow \Delta$ axial vector transition form factor, $G^A_{N\Delta}(Q^2)$. These measurements will allow $G^A_{N\Delta}(Q^2)$ to be mapped out without relying on PCAC and extrapolation of low energy theorems (as can be done in coincident pion electroproduction measurements near threshold), and free from the systematic and model dependent uncertainties associated with neutrino induced reactions. The parity violating $N \rightarrow \Delta$ asymmetry will provide direct access to this form factor, and the proposed measurements represent the first of this quantity in the neutral current sector of the weak interaction.

1 Introduction

The parity violating asymmetry measured in inclusive electron scattering reactions is driven by the exchange of a Z^0 boson, which can be exploited to probe hadronic structure. This feature has been the focus of much recent attention for elastic parity violating electron asymmetry measurements, both experimentally and theoretically, as a means for determining the contribution from strange quarks to ground state nucleon properties [1, 2, 3, 4]. Specifically, if isospin is taken to be a good symmetry, then parity violating elastic electron proton scattering directly probes the strange vector current matrix element $\langle p|\bar{s}\gamma_\mu s|p\rangle$, allowing for a determination of the nucleon strange charge and magnetic form factors, G^s_E and G^s_M. Experiments of this type are now technically quite feasible [5]. If parity violating electron nucleon scattering experiments are extended beyond the elastic channel into particular inelastic channels, additional information about the nucleon quark currents can clearly be obtained. Due to the pure isovector nature of the $N \rightarrow \Delta$ transition, the parity violating asymmetry in electroproduction of this resonance can isolate the isovector contributions to these currents [6, 7, 8, 9]. In particular, the axial vector transition form factor $G^A_{N\Delta}(Q^2)$, which has also been a topic of much recent experimental and theoretical interest [10, 11, 12, 13, 14], is isovector in nature, and can be directly accessed through the parity violating asymmetry in the $N \rightarrow \Delta$ transition.

Understanding the Δ resonance has always been considered an important test of nucleon structure models. Considerable effort continues to be put forth toward the measurement and interpretation of the $N \rightarrow \Delta$ electromagnetic transition form factors [15, 16, 17, 18]. Because the Δ can also be produced in electron scattering via the exchange of the neutral weak Z^0 boson, there are also weak transition form factors which contribute, including both vector and axial-vector pieces. Included in these isovector terms are the axial vector electron-vector quark and vector electron-axial vector quark contributions; the former depending only on the weak mixing angle $\sin^2\theta_W$, and the latter containing the axial transition form factor $G^A_{N\Delta}$. Given the success of the standard model of electroweak interactions [19, 20], the isovector couplings can be taken as input from the standard model, allowing for a determination of $G^A_{N\Delta}$ from these asymmetry measurements. In addition, it has been shown [7] that in the intermediate energy regime (E $\leq$ 1 GeV) and at large electron scattering angles, where we propose to make these measurements, the sensitivity of the parity violating asymmetry on $G^A_{N\Delta}$ is much larger than in the high energy limit ($\frac{Q^2}{2ME} \ll 1$), where this contribution to the asymmetry is negligible [6].

What is intriguing about the $N \rightarrow \Delta$ asymmetry measurements is that they provide direct access to $G^A_{N\Delta}$, and represent the first determination of this form factor in the neutral current sector of the weak interaction. In addition, this new physics has the distinct advantage that much of it can be obtained with minimal addition to existing apparatus, and with no additional beam time. In the TJNAF PAC approved G0 experiment [1], the parity violating asymmetry in elastic $\vec{e}+p$ scattering will be measured in two different modes of running. The superconducting toroidal spectrometer used for these measurements will be oriented in two directions: one for the detection of the forward scattered protons, and the other for the backward scattered electrons. Both configurations are necessary for the separation of G^s_E and G^s_M from the $\vec{e}+p$ elastic asymmetry measurements. In addition to the Focal Plane Detectors (FPD's), a set of detectors mounted at the exit of the G0 cryostat (Cryostat Exit Detectors) is required for the separation of the elastic and inelastic channels during the backward angle measurements. The coincidences between these two sets of detectors serve the dual purpose of eliminating the inelastic contamination from the elastic measurements, and allow the parity violating asymmetry to be mapped out across the Δ resonance simultaneously. The asymmetry in the $N \rightarrow \Delta$ transition is expected to be approximately the same size as that in elastic $\vec{e}+p$ scattering [8], and the inelastic yield is much larger but spread out kinematically; thus, similar statistical precision will be obtained for the inelastic asymmetry as for the elastic asymmetry during the same running period.

In addition, making measurements on two physical processes simultaneously can provide useful information. Information from both reactions can be used to check internal consistency in the experimental apparatus and on the measurement technique. In the case considered here, the differential cross section will be measured for both elastic $\vec{e}+p$ scattering and for electroproduction of the Δ. Because the differential cross sections for these two reactions are well known in this Q^2 regime, an excellent check on the spatial dependence of the detector efficiency will be contained in the data. It should be emphasized that these proposed measurements are possible due to the large acceptance of the G0 spectrometer. Although designed for optimum resolution and acceptance in the elastic channel, this device has the capability of simultaneously including the full width of the Δ resonance in its acceptance over a wide range of kinematic conditions.

2 Formalism

The coupling of electrons to quarks in the nucleon through the exchange of a Z^0 boson can be seen in Fig. 1, where we show the first order Feynman diagram for this exchange between an electron with four momentum K and target nucleon with four momentum P.

The momentum of the scattered electron is K', and the momentum and of the other outgoing

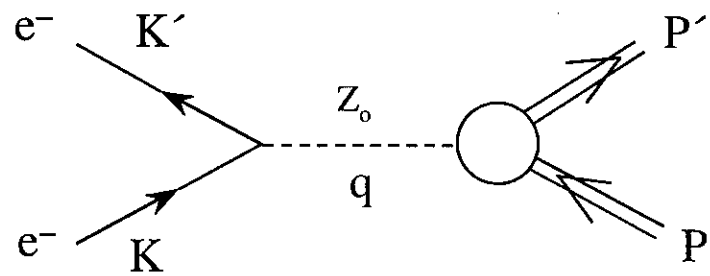

Figure 1: Feynman diagram for Z^0 exchange

particle is P'. The electron couples to the Z^0 boson according to

$$\langle K'|j_\mu^Z|K\rangle \;=\; \bar{u}(K')[g_{V,e}\gamma_\mu + g_{A,e}\gamma_\mu\gamma_5]u(K) \tag{1}$$

showing explicitly the vector-axial vector structure of the weak neutral current interaction. The vector and axial-vector couplings ($g_{V,e}$ and $g_{A,e}$) are functions of standard model parameters, given in Appendix A.

For the Z^0-nucleon coupling, the weak neutral current takes on different forms for the elastic and inelastic channels. In the elastic channel, we have

$$\langle P'|J_\mu^Z|P\rangle \;=\; \bar{u}(P')[\gamma_\mu F_1^Z + i\frac{\sigma_{\mu\nu}q^\nu}{2M}F_2^Z + \gamma_\mu\gamma_5 G_A^Z]u(P) \tag{2}$$

where, again, the vector-axial vector nature of the weak neutral current is evident. The neutral weak vector (F_1^Z,F_2^Z) and axial vector (G_A^Z) form factors of the nucleon (which are functions only of Q^2) can be expressed in terms of the individual quark form factors [4]; it is through these weak neutral form factors that the strange quark content of the nucleon can be accessed.

In the inelastic Δ channel, the neutral current is somewhat more complicated in its general form [8],

$$\langle P'|J^Z_\mu|P\rangle = \bar{U}^\lambda(P')[(\frac{C^Z_{3V}}{M}\gamma^\nu + \frac{C^Z_{4V}}{M^2}P'^\nu + \frac{C^Z_{5V}}{M^2}P^\nu)(g_{\lambda\mu}g_{\rho\nu} - g_{\lambda\rho}g_{\mu\nu})q^\rho\gamma_5 + C^Z_{6V}g_{\lambda\mu}\gamma_5$$
$$+(\frac{C^Z_{3A}}{M}\gamma^\nu + \frac{C^Z_{4A}}{M^2}P'^\nu)(g_{\lambda\mu}g_{\rho\nu} - g_{\lambda\rho}g_{\mu\nu})q^\rho + C^Z_{5A}g_{\lambda\mu} + \frac{C^Z_{6A}}{M^2}P_\lambda q_\mu)]u(P) \quad (3)$$

but the vector-axial vector nature can still be seen. In this expression, $U^\lambda(P')$ is the Rarita-Schwinger field describing the spin-$\frac{3}{2}$ Δ resonance [22], P and P' are, respectively, the momenta of the nucleon and the Δ, and $q = P' - P$.

The weak transition form factors in Eq. (3), which are functions only of Q^2, can be related to the electroproduction and weak charged current production of the Δ by performing a rotation in isospin space and exploiting the conserved vector current (CVC) hypothesis [8]. In the notation of Llewellyn-Smith [23], they become

$$\begin{aligned} C^Z_{iV} &= \alpha C^\gamma_i, \quad i = 3,4,5\,, \\ C^Z_{6V} &= 0\,, \\ C^Z_{iA} &= -\beta C^A_i, \quad i = 3,4,5,6\,, \end{aligned} \quad (4)$$

where α and β are the quark-Z^0 couplings (given in Appendix A). The electroproduction form factors are denoted by C^γ_i, and the C^A_i are $-\frac{1}{\sqrt{3}}$ times the charged-current axial vector weak transition form factors.

To make the isospin structure of this transition evident, it is useful to examine the parity violating phenomenological Lagrangian for electron nucleon scattering [24],

$$L = -\frac{G_F}{2}\{\bar{e}\gamma_\lambda\gamma_5 e[\frac{\tilde{\alpha}}{2}(\bar{u}\gamma_\lambda u - \bar{d}\gamma_\lambda d) + \frac{\tilde{\gamma}}{2}(\bar{u}\gamma_\lambda u + \bar{d}\gamma_\lambda d)]$$
$$+\bar{e}\gamma_\lambda e[\frac{\tilde{\beta}}{2}(\bar{u}\gamma_\lambda\gamma_5 u - \bar{d}\gamma_\lambda\gamma_5 d) + \frac{\tilde{\delta}}{2}(\bar{u}\gamma_\lambda\gamma_5 u + \bar{d}\gamma_\lambda\gamma_5 d) + ...]\}, \quad (5)$$

where $(\bar{e}, e)$, $(\bar{u}, u)$, and $(\bar{d}, d)$ represent Dirac spinors for the electrons and quarks, the electron-quark coupling constants have the following meaning:

$\tilde{\alpha}$: isovector axial vector electron – vector quark,

$\tilde{\beta}$: isovector vector electron – axial vector quark,

$\tilde{\gamma}$: isoscalar axial vector electron – vector quark,

$\tilde{\delta}$: isoscalar vector electron – axial vector quark,

with standard model relations

$$\tilde{\alpha} = -(1 - 2\sin^2\theta_W)$$

$$\tilde{\beta} = -(1 - 4\sin^2\theta_W)$$

$$\tilde{\gamma} = \frac{2}{3}\sin^2\theta_W$$

$$\tilde{\delta} = 0.$$

The dots in Eq. (5) denote isoscalar axial heavy quark (s,c,...) currents.

Because the $N \to \Delta$ transition is purely isovector, the parity violating asymmetry for Δ production takes the form [7]

$$A_{RL} = \frac{d\sigma_R - d\sigma_L}{d\sigma_R + d\sigma_L} = \frac{G_F}{\sqrt{2}}\frac{Q^2}{2\pi\alpha}[\tilde{\alpha} + \tilde{\beta}F(Q^2, E, E', \theta_e)], \quad (6)$$

where $d\sigma_{R(L)} \equiv \frac{d^2\sigma}{dq^2 dW^2}|_{R(L)}$ is the differential cross section for scattering electrons of positive (negative) helicity from the nucleon, $Q^2 = -(K-K')^2$, $W^2 = (P+K-K')^2$, α in this case is the electromagnetic coupling constant, and $F(Q^2, E, E', \theta_e)$ contains all of the weak transition form factors discussed above, in addition to dependence on kinematic variables. Specifically, we write (see Appendix A),

$$F(Q^2, E, E', \theta_e) \;=\; \frac{(E+E')}{M} H^{EM}(Q^2, \theta_e) G^A_{N\Delta}(Q^2), \tag{7}$$

where $H^{EM}(Q^2, \theta_e)$ contains the electromagnetic form factors $C_i^\gamma(Q^2)$ $(i = 3,4)$ (which will be more precisely determined in future Hall B experiments), and $G^A_{N\Delta}(Q^2)$ contains the axial transition form factors $C_i^A(Q^2)$ $(i = 3,4,5,6)$. Thus, for a pure isovector $N \to \Delta$ transition, the parity violating asymmetry consists of two terms: the axial vector electron-vector quark coupling, which is given explicitly by the electron-quark coupling constant $\tilde{\alpha}$, and the vector electron-axial vector quark coupling, which contains the axial vector transition form factor $G^A_{N\Delta}$. The relative strengths of these two terms is determined by the coupling constants $\tilde{\alpha}$ and $\tilde{\beta}$, which, with the standard model value of $\sin^2\theta_W$=0.2236, take on the numerical values

$$\tilde{\alpha} \;=\; -0.5536 \;\;,\;\; \tilde{\beta} \;=\; -0.1056.$$

Thus, for reasonable $F(Q^2, E, E', \theta_e)$ values, the leading $\tilde{\alpha}$ term contributes roughly 75% to this parity violating asymmetry. Using estimates for the $N \to \Delta$ weak transition form factors, $F(Q^2, E, E', \theta_e)$ is found to be of order unity in this kinematic regime [7], in contrast to the high energy limit ($\frac{Q^2}{2ME} \ll 1$), where $F(Q^2, E, E', \theta_e) \ll 1$ [6]. Consequently, using relatively low beam energies and detecting electrons scattered at backward angles will enhance our sensitivity to the $N \to \Delta$ axial transition form factor $G^A_{N\Delta}(Q^2)$.

This form factor can be accessed in a number of different ways, and is usually parameterized in terms of the axial-vector mass M_A, according to the Adler model [25], in which a modified dipole form is used. In neutrino induced weak Δ^{++} production, $G^A_{N\Delta}(Q^2)$ can be determined through the Q^2 dependence of the differential cross section for this reaction, and therefore represents a determination of this form factor in the charged current sector of the weak interaction. An early study of neutrino induced weak Δ^{++} production from the proton [26] yielded a value of $M_A = 0.95 \pm 0.09$. A more recent study [27] of this reaction on deuterium between $0.1 \leq Q^2 \leq 3.0$ (GeV/c)^2 yielded $M_A = 1.28^{+0.08}_{-0.10}$, but this value showed sensitivities to deuteron structure and cuts on spectator nucleon momentum. The measurements described in this proposal will provide the first determination of M_A in the neutral current sector. Comparison between these two types of measurements of the same physical quantity can therefore provide us with an indication of how important isospin breaking corrections are in the weak interaction [31]. In $\pi^-\Delta^{++}$ electroproduction, coincidence differential cross section measurements are typically performed near threshold [14, 28, 29], in which the scattered e^- and the electroproduced π^- are detected. To interpret these data, low energy theorems are extrapolated from threshold through the resonance region, and use is made of the partially conserved axial vector current (PCAC) hypothesis. To date, data from experiments of this type have instead been interpreted, using the theoretical results of Adler and Weisberger [30], in terms of the nucleon axial vector form factor $G_A(Q^2)$. The TJNAF PAC approved E94-005 experiment [14], however, will use the above mentioned techniques and approximations to extract $G^A_{N\Delta}$ for larger Q^2 values than considered in this proposal ($0.5 \leq Q^2 \leq 2.5$ (GeV/c)^2). In contrast, the measurement of the parity violating asymmetry in the $N \to \Delta$ transition proposed here gives direct access to $G^A_{N\Delta}(Q^2)$, without PCAC or extrapolation of low energy theorems. Because PCAC, which essentially states that all of the axial current is carried away by the electroproduced π^-, is expected to be broken at the 5-7% level [31], comparison of the determination of

$G^A_{N\Delta}(Q^2)$ from the electroproduction experiments with the determination through the parity violating asymmetry in the $N \rightarrow \Delta$ transition can provide some insight into PCAC violation.

Although these asymmetry measurements give us direct access to $G^A_{N\Delta}(Q^2)$, a correct determination of this form factor can only be done if the non-resonant contributions to the asymmetry are small, or understood. With an extensive data base of single pion photoproduction cross section measurements in the region of the Δ [32, 33, 34, 35, 36, 37], a model independent determination of the resonant and non-resonant contributions to this process has been made [38], allowing for a determination of the $E2/M1$ ratio for the resonance, free from uncertainties associated with theoretical models of background contributions. This ratio, recognized early on as a crucial quantity to test theories of effective forces between quarks needed to understand hadron structure [39], could be extracted with no model dependence, allowing for a cleaner interpretation of the data and their implications for theoretical models. While it is true that the allowed phase space for inclusive single π electroproduction from the proton has its dominant contribution from the resonant Δ^+, there are contributions from non-resonant processes which must be understood for a proper interpretation of the data (see Appendix B). To understand these contributions to the asymmetry, a similar model independent determination of the resonant and non-resonant pieces must be performed throughout the entire Q^2 range studied. Several measurements planned for Hall B [40] will address this issue directly by mapping out the Q^2 dependence of both resonant and non-resonant multipoles in single π electroproduction for $Q^2 \leq 4$ (GeV/c)^2. Although these experiments focus on determining the electromagnetic ratio $\frac{E_{1+}}{M_{1+}}$ to high precision (errors of order 0.005), the combination of angular distributions and polarization observables will allow for determinations of all of the s and p wave multipoles, along with their isospin decomposition, to somewhat less precision (errors of order 0.04) [40].

Until such electroproduction data exist to constrain the non-resonant multipoles, we must rely on models for an estimate of what contribution the non-resonant background will make to the parity violating asymmetry in the $N \rightarrow \Delta$ transition. One such estimate can be made by comparing two calculations of this asymmetry: one for pure Δ production [8], and one for single π production at the same energy [41], which includes contributions from all Born diagrams and ρ and ω meson contributions in addition to the Δ. These two calculations are within 10% of each other in the Q^2 range considered in this proposal, suggesting that the contribution to the asymmetry from the non-resonant background is indeed small in this kinematic regime. More recently, a phenomenological model with effective Lagrangians [13] was used to calculate the parity violating asymmetry in π electroproduction from the proton in the energy region between pion threshold through the Δ resonance. In these results, contributions from the resonant, non-resonant, and interference terms are given separately as a function of both Q^2 and k_γ (photon equivalent energy), providing a useful guide for understanding the sensitivity of the asymmetry to these separate contributions in varying kinematic regimes. In Fig. 2 we show the calculations of Ref. [13] near the peak of the Δ resonance for these different contributions to the asymmetry at an incident beam energy of 0.8 GeV, normalized to the Q^2 of the reaction, as a function of Q^2, along with our expected statistical uncertainty for the inelastic $\vec{e} + p$ measurements to be made concurrent with the G0 elastic $\vec{e} + p$ measurements. As in the previous estimate based on the calculations of Ref.'s [8] and [41], the full calculation and the resonant contribution differ by at most 10% in this same Q^2 regime, giving us confidence that a meaningful interpretation of these data is possible. With the non-resonant contributions sufficiently constrained, we can make an estimate of what precision we can achieve on the axial transition form factor $G^A_{N\Delta}$, which we plot in Fig. 3, using the modified dipole parameterization of Adler [25]. From the expected statistical precision, we can extract the axial mass M_A from $G^A_{N\Delta}$ with an absolute error of 0.03, roughly a factor of 3 better than any of the neutrino experiments which have extracted this parameter.

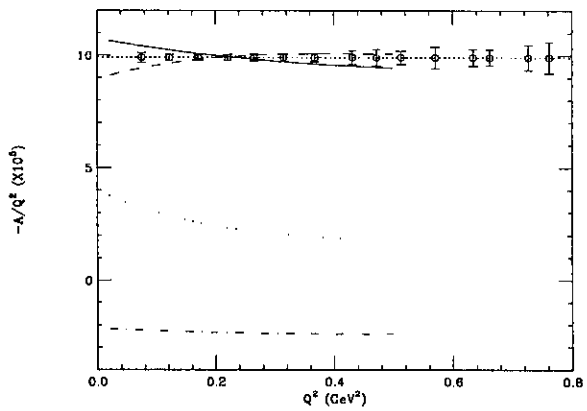

Figure 2: Asymmetries for the $\vec{e} + p$ inelastic reaction at the peak of the Δ resonance. The result of the full calculation (solid line) is compared to the contributions of the non-resonant background (dotted line), resonance (long dashed line), resonance neglecting the contribution from the axial form factor $G^A_{N\Delta}(Q^2)$ (short dashed line), and interference term (dot-dashed line). Included are the expected statistical uncertainties of our measurements in the several Q^2 bins of the reaction to be measured.

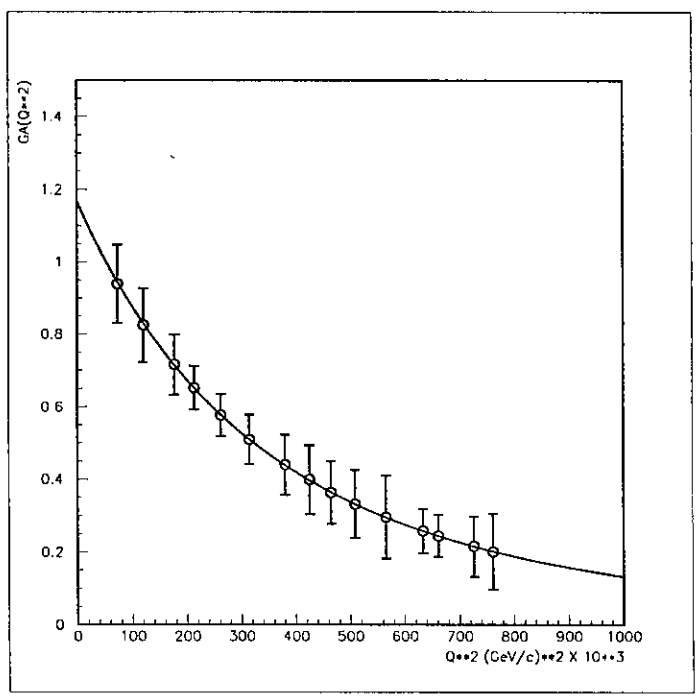

Figure 3: Axial vector transition form factor $G^A_{N\Delta}$ plotted vs. Q^2 assuming the Adler parameterization. Errors represent expected statistical errors only, and the allowed kinematical region for 2-π production has been excluded.

3 Kinematics and Cross Section Calculation

The design of the $N \rightarrow \Delta$ transition experiment in this proposal has several constraints which have already been taken into account. The G0 spectrometer and associated collimator design is optimized for elastic forward proton and backward electron scattering, and can be used for the $N \rightarrow \Delta$ transition asymmetry measurements with no modification. For these inelastic asymmetry measurements made during the same running period that the elastic electron-proton asymmetry measurements are made, we can not alter any of the G0 spectrometer settings.

The asymmetry in the $N \rightarrow \Delta$ channel will be measured with the G0 spectrometer in the backward angle measurement mode. In this configuration, elastically scattered electrons are detected in an angular range centered around $\theta_e \sim 110°$. Using the magnetic field setting, target position and target length for the elastic channel settings, we can calculate the kinematical limits for the inelastic electrons, which are shown in Table 1.

The measurement of the $N \rightarrow \Delta$ asymmetry using the G0 spectrometer is an inclusive measurement, in which only inelastically scattered electrons are detected. The calculation of the cross section in this kinematical range is based partially on the work of J. W. Lightbody and J.S. O'Connell [42] and F.W. Brasse *et al.* [43, 44]. The inelastic electron scattering cross section is calculated as the product of the virtual photon flux and the total cross section for virtual photon-proton scattering, as a function of Q^2 of the virtual photon and the invariant mass of the photon-proton system. The calculation of the total cross section for virtual photon-proton scattering is based on the parametrization by Brasse *et al.* [43, 44]. The results for some electron angles are shown in Fig. 4 for an electron beam momentum of E=0.933 GeV.

$E(GeV)$	$Q^2_{el.}((GeV/c)^2)$	$Q^2_{inel.}((GeV/c)^2)$	$E'_{inel.}$ (GeV)	$\theta'_{inel.}(deg)$
0.585	0.5	0.04 - 0.38	0.066 - 0.259	57.3 - 111.7
0.730	0.7	0.05 - 0.56	0.073 - 0.307	56.3 - 113.5
0.933	1.0	0.10 - 0.82	0.082 - 0.362	55.0 - 114.6

Table 1: Inelastic kinematics for magnetic fields optimized for the elastic channel, calculated for three beam energies.

The calculation of the Δ electroproduction cross section for the beam energies below 1 GeV is in good agreement with the existing data [42], and can be used to estimate the rates and uncertainties for the $N \rightarrow \Delta$ asymmetry measurements.

4 Rates

The rates for the inelastically scattered electrons are calculated as:

$$Rates = \int_{E'_{min}}^{E'_{max}} \int_{\Delta\Omega} \frac{d\sigma}{dE' d\Omega} dE' d\Omega \tag{8}$$

where $\frac{d\sigma}{dE' d\Omega}$ is the double differential inelastic electron cross section, E'_{min} and E'_{max} are the lower and upper limits of the detected electron momentum, and $\Delta\Omega$ is the covered solid angle. For the inelastic channel, the scattered electron momentum range $\Delta E'$ and solid angle $\Delta\Omega$ are small enough in each Focal Plane Detector-Cryostat Exit Detector coincidence measurement to allow Eq.(8) to be replaced by:

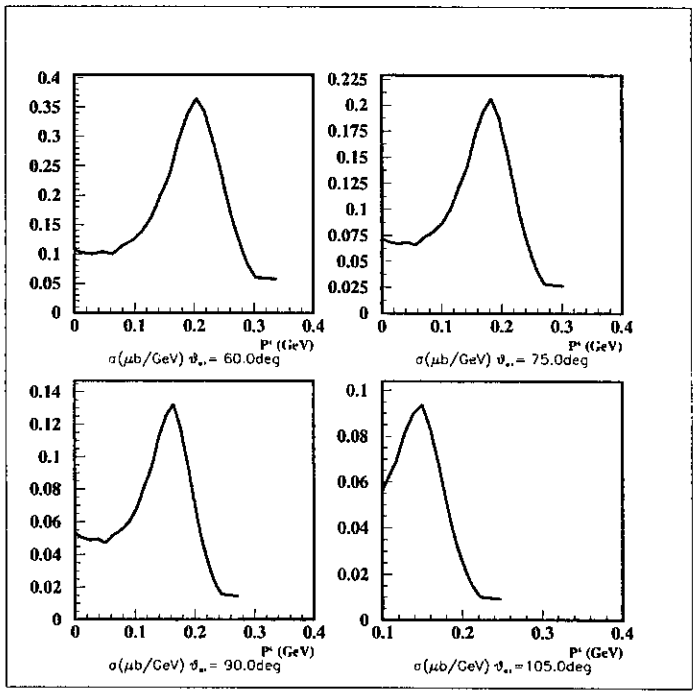

Figure 4: Inelastic electron-proton cross section calculations for E=0.585 GeV, at four electron scattering angles.

$$Rates = \overline{\frac{d\sigma}{dE'd\Omega}}\,\Delta E'\,\Delta\Omega, \tag{9}$$

where $\overline{\frac{d\sigma}{dE'd\Omega}}$ is the average inelastic electron cross section for electrons having a momentum range $\Delta E'$ detected in the solid angle $\Delta\Omega$.

The measurement of the $N \rightarrow \Delta$ channel in these measurements is broken into hundreds of $\Delta\Omega$ and $\Delta E'$ bins, depending on the number of Focal Plane Detectors and Cryostat Exit Detectors used in the experiment. The analysis of rates is done by assuming coincidences between 12 Cryostat Exit Detectors and 16 Focal Plane Detectors. The total number of possible FPD-CED coincidence combinations is 192, but due to the allowed phase space for single pion production, a little less than half of these are used for the $N \rightarrow \Delta$ measurement.

The procedure for the rate calculation can be divided into several steps:

- for the single pion production reaction, the phase space density of the three particle final states is calculated numerically using the CERN library routine GENBOD [45]
- the inelastically scattered electrons are tracked through the G0 spectrometer by the program TRACKTOR, part of the program package used for the spectrometer design [46, 47]
- electron multiple scattering is calculated in the liquid hydrogen target using a Gaussian multiple scattering method [48]
- the electron momentum range and solid angle are calculated from the Monte Carlo simulation as twice the standard deviation of the appropriate distributions obtained by requiring that the electrons generated in the target track through a particular Cryostat Exit Window Detector segment and particular Focal Plane Detector segment
- beam current, target length and thickness, and luminosity are assumed to be the same as for the elastic scattering experiment [47], and are represented in Table 2.

Average current:	40 μA
Target length:	Q^2 dependent (10-20 cm)
Luminosity:	Q^2 dependent ($1.05 - 2.1 \times 10^{38}\ cm^{-2}s^{-1}$)

Table 2: Beam and target parameters for luminosity determination.

Some results from the procedure described can be seen for a beam energy E=0.933 GeV in Fig.'s 5 and 6, where the scattered electron momentum and angle, respectively, are shown for the Δ resonance in the space of Focal Plane Detector-Cryostat Exit Detector coincidences. These plots show that the spectrometer and detector acceptance can include the full width of the Δ in FPD-CED coincidence space.

Finally, calculated rates for the same beam energy E=0.933 GeV are shown in Fig. 7.

5 Statistical Uncertainties of the Measured Asymmetries

In the previous two sections, we have described a procedure for calculating inelastically scattered electron kinematics, cross section and counting rates for particular CED segment-FPD segment coincidences. The asymmetry is then determined from yields for the two beam helicities (each measured for a time T_h) as [47]:

$$A^{meas} = \frac{Y_+ - Y_-}{Y_+ + Y_-}, \tag{10}$$

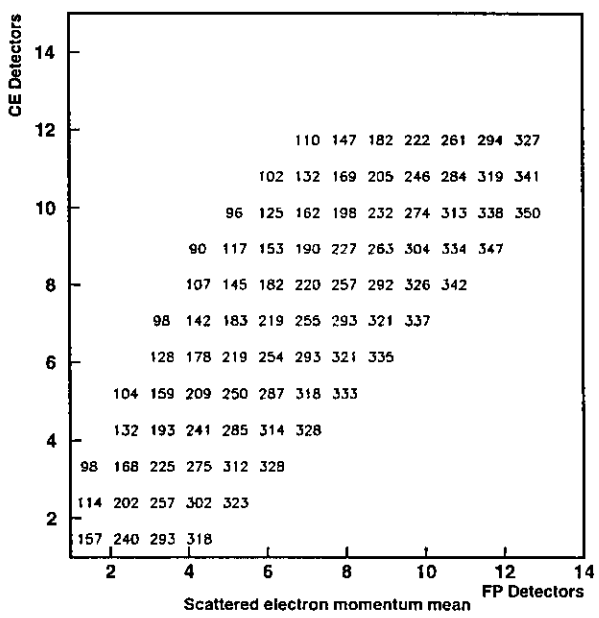

Figure 5: Scattered electron momentum (in MeV) in FPD-CED space for E=0.933 GeV. As an example, the distribution of coincidences between CED number 4 and FPD number 6 has a mean momentum of 314 MeV.

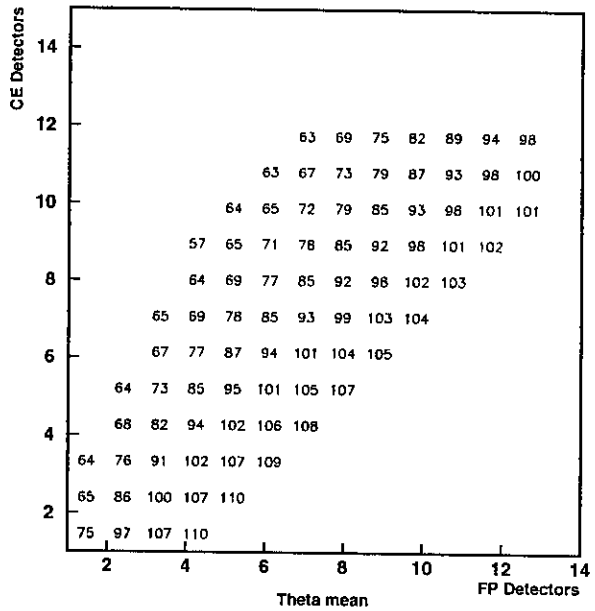

Figure 6: Scattered electron angle (in degrees) with associated standard deviation in FPD-CED space for E=0.933 GeV.

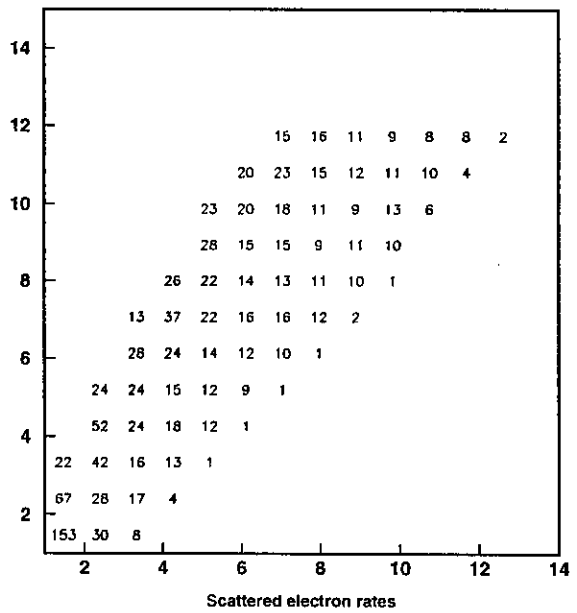

Figure 7: Inelastic electron counting rates (in kHz) in FPD-CED space for E=0.933 GeV.

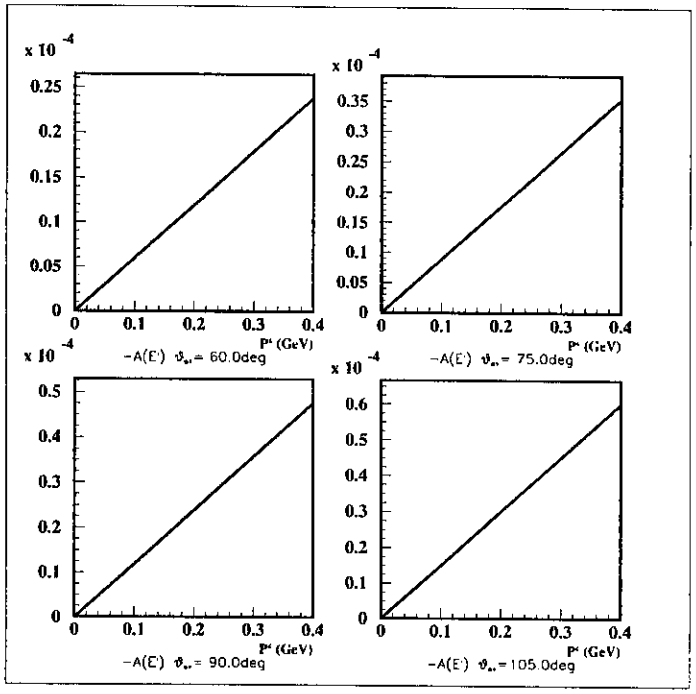

Figure 8: Expected asymmetry as a function of scattered momentum for four electron scattering angles for E=0.933 GeV.

where

$$Y_h = \frac{Rate \times T_h}{Q_h} = \frac{N_h}{Q_h}, \tag{11}$$

and N_h and Q_h are the total number of counts in the detectors and the beam charge passing through the target in time T_h, respectively.

The number of counts in the detectors for the two beam helicities is approximately equal, $N_+ \simeq N_- = N/2$, where N is the total number of counts. Neglecting, for now, any dilution factor, the statistical uncertainty we expect to achieve is simply:

$$\Delta A^{meas} = \frac{1}{\sqrt{N}}. \tag{12}$$

While a detailed description of the $N \rightarrow \Delta$ transition asymmetry is given in previous sections and the appendices, to calculate the statistical precision of the proposed measurement, we use only the dominant leading term in the asymmetry,

$$A = \frac{G_F}{\sqrt{2}} \frac{Q^2}{2\pi\alpha} \tilde{\alpha}, \tag{13}$$

where Q^2 is the four momentum transfer squared, $G_F = 1.17 \times 10^{-5}(\mathrm{GeV}^{-2})$ is the Fermi coupling constant, $\alpha = 1/137.04$ is the electromagnetic coupling constant, and $\tilde{\alpha}$ is taken to be -0.5536 (with the standard model value of $\sin^2\theta_W = 0.2236$). An example of asymmetries calculated using this formula are shown in Fig. 8.

$E(GeV)$	Time (h)	Target length (cm)	$Q^2_{\text{inel.}}$ Range ($(GeV/c)^2$)	$\overline{\frac{\Delta A}{A}}/Bin$	No. of bins
0.585	700	20	0.04 - 0.38	21 %	80
0.730	700	12	0.05 - 0.56	31 %	82
0.933	700	10	0.10 - 0.82	21 %	85

Table 3: Kinematic Ranges and Statistical Precisions for Inelastic Measurements

The expected statistical uncertainties for inelastic asymmetry measurements made during the same running period as the elastic asymmetry measurements are summarized in Table 3 for three beam energies. The running time for each measurement is assumed to be 700 hours.

In Table 3, each bin corresponds to a particular FPD-CED coincidence, with a mean value of Q^2 for that bin at that beam energy. To determine the expected statistical accuracy for each Q^2 bin (with full width 0.05 GeV), we take the weighted average of the expected uncertainties of all the FPD-CED coincidence bins with mean Q^2 values within each 0.05 GeV Q^2 bin for all incident beam energies. These are the expected statistical uncertainties for the $N \rightarrow \Delta$ asymmetry shown in Fig. 2 as a function of Q^2. The same procedure is performed to obtain the expected statistical accuracy for $G^A_{N\Delta}$ shown in Fig. 3 as a function of Q^2, after excluding those FPD-CED coincidence bins which include the allowed kinematical region for 2-π production (described in Section 8).

6 Systematic Uncertainties and False Asymmetries

The G0 experiment is designed to measure the asymmetry in parity-violating elastic electron scattering from the nucleon $p(\vec{e}, e)p$ to 5% statistical accuracy in the Q^2 range between 0.1 and 1.0 (GeV/c)^2, where the expected asymmetry ranges from approximately -3.0×10^{-6} to -75.0×10^{-6}. Accordingly, limits on the systematic uncertainties have been set at 5% of the overall goal for the experiment [47], where limits on individual false asymmetries are set to be less than $5\% \times 2.5 \times 10^{-7} \simeq 1 \times 10^{-8}$.

Because the expected $N \rightarrow \Delta$ transition asymmetries are larger than the asymmetries in elastic electron scattering, the limits set for the systematic uncertainties and false asymmetries for the elastic case are more than adequate for the $N \rightarrow \Delta$ asymmetry measurement.

The helicity uncorrelated background noise is reduced by a data-taking sequence of a randomly chosen beam helicity pattern of four, $+ - -+$ or $- + +-$, where one helicity state is measured during the time interval $T_h = 1/30s$, assuming that long term drifts are essentially linear during such short time intervals. The local power deposited in the target by the high current beam is reduced by rastering the beam on the target.

The list of specifications of systematic uncertainties and false asymmetries taken from the G0 Technical Design Report [47] include:

- measurement of the average beam polarization to 2%
- measurement of the beam charge during the measurement time of $T_h = 1/30s$ to $\Delta Q/Q = 4 \times 10^{-5}$
- measurement of the parameters whose variations are correlated with helicity during the measurement time $T_h = 1/30s$ to the precision of:
  - beam energy $\Delta E/E = 1 \times 10^{-5}$

- beam diameter $\Delta d/d = 100\%$
- beam intensity $\Delta I/I = \Delta Q/Q = 4 \times 10^{-5}$
- beam position and angle $\Delta r = 800\mu m$ and $\Delta\theta = 14\mu rad$

In the G0 Technical Design Report, it was shown that the contribution to the false asymmetry from the nonlinear terms, deadtime, pileup, polarized proton scattering in the collimators and target, changes in beam shape, and particle counting are negligible, even on the level of the smallest expected asymmetry for the elastic measurements.

7 Hall C Beam Development

During a TJNAF running period in July and August of 1997, polarized beam was delivered to both Hall A and Hall C (Hall A being the priority hall). The efforts in Hall C, driven by many of the G0 Collaboration members, were directed toward measuring properties of the beam which depend on the beam helicity, and understanding the sensitivities of these properties to helicity. This was possible because the beam line from the beam switch yard through the transport arc to the Hall C target position was instrumented with Beam Position Monitors (BPMs), and Beam Current Monitors (BCMs) were installed near the Hall C target position. In addition, because sensitivities to helicity were being investigated, a copy of the signal determining the sign of the voltage applied to the helicity Pockels cell (thereby determining the "handedness" of the circular polarization of the light incident on the GaAs crystal, and therefore the polarization direction of the electron beam) was sent from the Polarized Source to the Hall C counting house.

Throughout this run, the beam helicity was reversed at 30 Hz in a non-random fashion. To obtain information on sensitivities to electronic noise, signals from each BPM and BCM, in addition to the helicity signal, were read out via CAMAC at 120 Hz. Four voltage signals from each BPM, corresponding to the left, right, top, and bottom electrodes, in addition to the voltage signals for the beam helicity and each BCM (corresponding to the total charge density of the beam at that position), were used as input to Voltage to Frequency (VtoF) converters, the outputs of which were fed into CAMAC scalers to be read and cleared every $\frac{1}{120}$ seconds. This was sufficient information to determine the horizontal and vertical beam position at several points along the Hall C beam line, and the total beam current incident on the Hall C target, averaged over each 7 ms counting interval. Because the helicity of the beam was also read during this time period, the average helicity correlated beam current difference, and the average helicity correlated horizontal and vertical beam position differences could be determined at several points along the beam line. In particular, one BPM was installed at a position where the beam dispersion is known (22mm/%), allowing the helicity correlated beam energy asymmetry to be deduced from the helicity correlated beam position difference at that point in the beam line.

Because Hall A was the priority hall during this run, properties of the beam could not be changed at our request. Our approach was to simply take the beam tune as given, and determine the beam sensitivity to helicity for this parasitic run. Once a satisfactory beam tune was established into Hall C, data taking ensued. Shown in Fig. 9 are some results from the first several hours of parasitic running. The horizontal and vertical beam position differences from the last two BPMs in the Hall C beam line (from which the helicity correlated beam position and angle differences can be determined), and beam charge and energy asymmetries are plotted as a function of Run Number (giving a good indication of how things are changing with time). As can be seen from the figure, simply turning on a parasitic beam into Hall C produces a beam with helicity correlated position and angle differences consistent with zero (at the 100 nm level), helicity correlated energy asymmetries consistent with zero (at the 10×10^{-6} or 10 part per million (ppm) level), and helicity correlated intensity modulations at the 10-20 ppm level. In

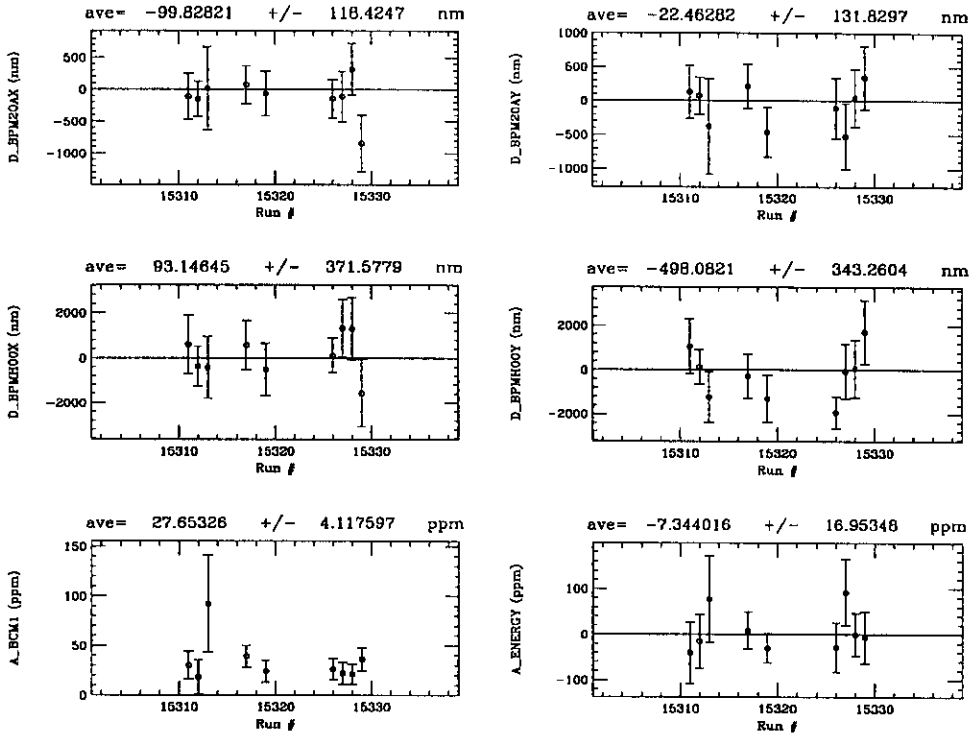

Figure 9: Helicity correlated beam position differences at BPMs $\sim$ 17 m (upper two: left - horizontal, right - vertical) and $\sim$ 6.5 m (middle two: left - horizontal, right - vertical) upstream of the Hall C target position, and helicity correlated beam charge (lower left) and energy (lower right) asymmetries, as a function of Run Number.

addition, the BCMs were shown to be sensitive to better than the 10^{-4} level, and the BPMs were shown to have intrinsic resolutions of less than 30 μm (with issues of common mode electronic noise to be resolved). Finally, to test what level of false asymmetry would be introduced by helicity correlations in the data acquisition electronics, data acquisition was enabled during time periods when beam was not being transported into Hall C. The combined asymmetry of these "pedestal" runs was consistent with zero to the 10^{-7} level. All of these results give us confidence that the systematic uncertainties and false asymmetries associated with the TJNAF beam will be small, and can be kept at a controlable level.

8 Background Consideration

In the presence of background, the measured asymmetry A_m is related to the inelastic asymmetry A_i by the following expression [47]:

$$A_m = \frac{A_i R_i + A_b R_b}{R_i + R_b} \tag{14}$$

where R_i and R_b (A_i and A_b) are the total counting rates (asymmetries) for the inelastic and the background events, respectively. The backward angle measurement of electrons is essentially free from background contamination (a discussion of the physics background of non-resonant terms can be found in Appendix B). In particular, the magnetic analysis of the G0 spectrometer and collimator system ensures that only negatively charged particles scattered from the target

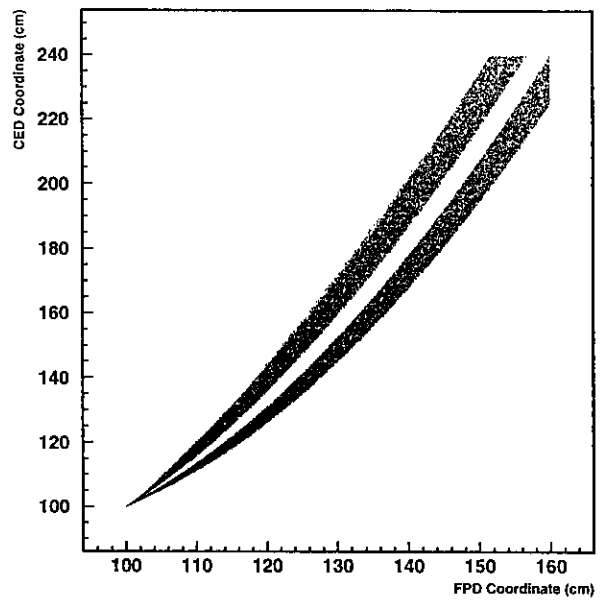

Figure 10: Elastic (lower band) and threshold inelastic (lower band) scattering loci in FPD-CED space.

will reach both sets of detectors. In addition, with the kinematics set by the G0 spectrometer, we can identify at what point the 2-π phase space opens up. Thus, by excluding the region above 2-π production threshold, the $e + p \rightarrow e'\Delta^{++}\pi^-$ cannot contribute. Because the beam energies chosen for the G0 elastic measurements are sufficiently low, the background in the inelastic asymmetry will come mainly from the elastic channel, in addition to enhancing the sensitivity of the inelastic asymmetry to the $G^A_{N\Delta}$ form factor. From kinematics alone, a significant energy gap exists between the elastic and inelastic electrons in CED-FPD space which allows a clean separation between these two channels. An example of such a gap is shown in Fig. 10 for an electron beam energy of E=0.730 GeV and target length L =10 cm.

Due to the finite length of the LH_2 target, however, the incident beam electrons can lose energy (radiating bremsstrahlung photons) before scattering from a target proton. There will therefore be an elastic "radiative tail" which will contaminate the inelastic measurement. The yield for this process can be estimated by knowing how the cross sections for bremsstrahlung and elastic scattering depend on electron and photon energy [49]. Because these measurements will be performed with different beam energies, different amounts of the elastic radiative tail will contribute, depending on which beam energy is used. In the worst case, corresponding to the lowest beam energy, we estimate that the yield from this contamination is of order 1% of the inelastic pion production yield. In addition, the elastic parity violating asymmetry will be measured, allowing us to calculate the contribution to the inelastic asymmetry from this background process. Thus, we conclude that the contribution from the elastic radiative tail to the asymmetry in the inelastic channel is small, and easily correctable.

The neutron background in the backward direction will consist mainly of a low energy neutron

gas, the rate of which is expected to be a factor of two smaller than in the forward direction [47]. This neutron background has been extensively studied using a GEANT simulation [50], and special emphasis has been placed on the design of neutron shielding for the detector system. With this shielding design, the expected neutron background will be small enough that the false asymmetry due to accidental FPD-CED coincidences will be negligible, even if the asymmetry of the neutron background is several times larger than the asymmetry of interest [47]. (This neutron background contribution can be estimated by measuring rates with the spectrometer magnetic field off.)

The elastic electron-proton experiment is designed so that both background asymmetries and rates will contribute at most 5% to even the smallest elastic scattering asymmetry. Because both the rates and expected asymmetry for the $N \rightarrow \Delta$ transition are higher, the designed experimental apparatus will allow the $N \rightarrow \Delta$ asymmetry measurement to be made with even less dilution from background than in the elastic case.

In addition, special attention has been given to the 2-π final state channel. The impact of this background on the $N \rightarrow \Delta$ asymmetry measurement depends on the kinematical overlap of these two different channels, as well as on the cross section for 2-π production. The kinematical overlap is a function of the beam energy and increases with increasing beam energy. The kinematical limits of the 2-π final state channel for a few selected beam energies are shown as lines in Fig. 11, where the 2-π final state allowed kinematical region is above the line.

From Fig. 11, we can see that the kinematical region contaminated by the 2-π final state reaction is small for lower beam energies, but becomes roughly 50% at the highest beam energy. In our first conservative approach, only data from the uncontaminated region will be used. Extraction of the data from the contaminated region can later be performed by using two pion production cross section values and estimates of the parity violating asymmetry in this channel, which presently do not exist. It is expected (see Fig.'s 2 and 17, and Ref. [13]) that the parity violating asymmetry in single pion electroproduction varies smoothly and slowly as a function of both Q^2 and excitation energy. Any sharp deviation from this dependence at the 2-π threshold would indicate that something unexpected occurs at the opening of this channel.

9 Experimental Apparatus

Although the experimental apparatus described here is designed for the elastic electron-proton channel, it can be used for the $N \rightarrow \Delta$ asymmetry measurement with no modification. While here we present only the essential properties of selected parts of the apparatus, a very detailed description can be found in G0 Technical Design Report [47]. Measurements of asymmetries as small as -3×10^{-6} with statistical uncertainties of $\Delta A/A \leq 5\%$ and systematic uncertainties related to helicity correlated effects of $\Delta A \leq 2.5 \times 10^{-7}$ in a reasonable amount of time requires high luminosity and a large-acceptance spectrometer and detector system.

The large-acceptance is achieved by a magnetic spectrometer, consisting of a toroidal array of eight superconducting coils with a field integral of approximately 1.6 T·m. The spectrometer is designed to focus particles of the same momentum and scattering angle from the length of the extended target to a single point, *i.e.*, zero magnification in the dispersion direction [47]. The maximum momentum of the spectrometer is chosen to match the maximum proton momentum of $\sim$ 800 MeV/c for the forward elastically scattered protons. In the backward direction, the elastically scattered electrons can be efficiently measured using beam energies up to 2.2 GeV. The overall acceptance of the spectrometer for the elastically scattered electrons in this latter configuration is 0.5 - 0.9 sr.

Because the magnetic spectrometer is going to be used for small asymmetry measurements, special attention in the design has been put into:

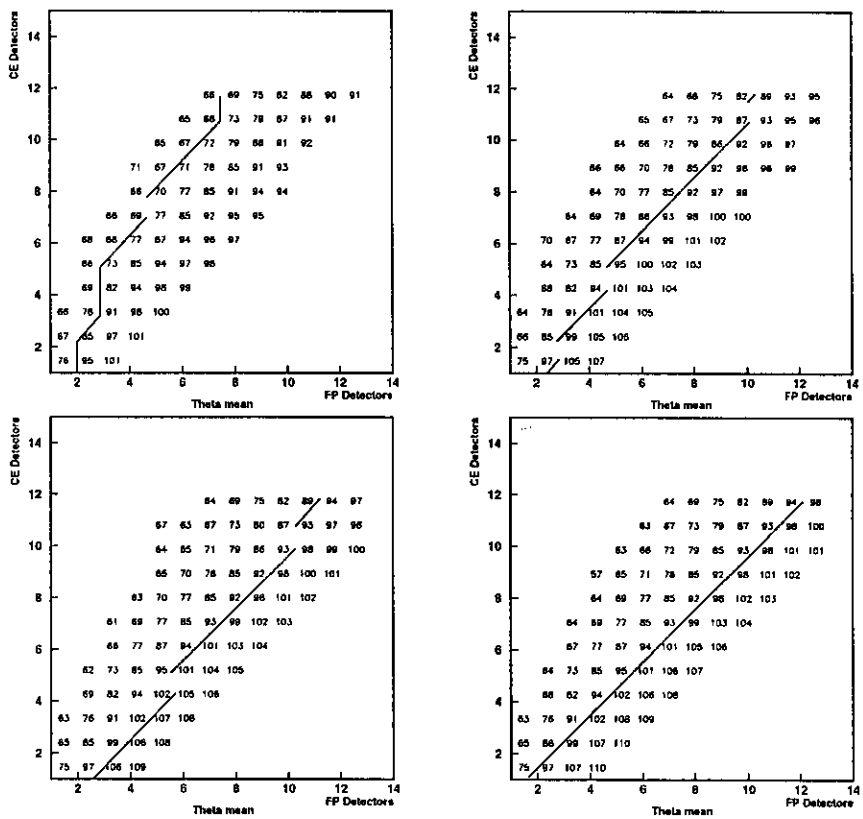

Figure 11: Allowed phase space for 2-π production (above the line) in FPD-CED space, for four different beam energies.

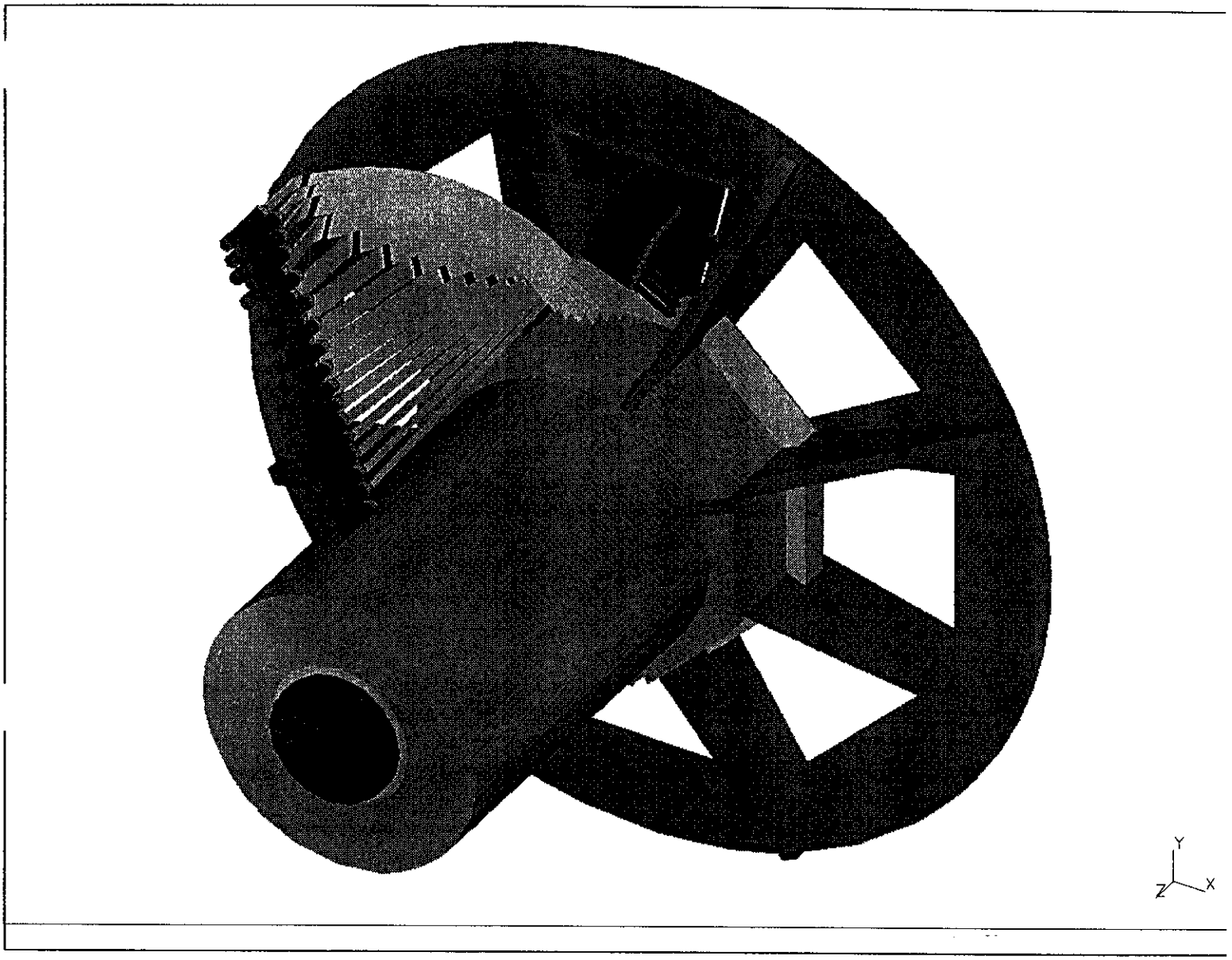

Figure 12: Schematic view of major experimental apparatus components.

- azimuthal symmetry of the spectrometer, minimizing the sensitivity to systematic errors associated with the beam motion
- not having magnetized iron in the spectrometer, therefore eliminating false asymmetries due to secondary scatterings
- having zero magnetic field at the target position
- making it a stand-alone device, thus providing a stable setup, important for asymmetry measurements
- making the spectrometer small enough to be positioned upstream of the pivot in Hall C for minimal interference with other experiments.

The detector is composed of a system of scintillator detectors, each viewed by two photomultiplier tubes, one attached at each end through a light guide. It consists of two sets of detectors:

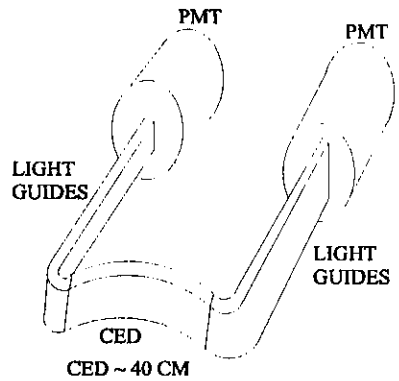

Figure 13: Schematic of an individual Cryostat Exit Detector, including attached light guides and photomultiplier tubes.

16 Focal Plane Detectors and 12 Cryostat Exit Window Detectors, both shown schematically in Fig. 12 (where, for clarity, only one of the 8 G0 sectors is shown, and only one light guide and photomultiplier tube are shown for each detector). The detectors are designed for two main purposes: the Focal Plane Detectors will detect protons scattered in the forward direction and separate them according to the Q^2 bins of the reaction; and both Focal Plane and Cryostat Exit detectors will detect electrons scattered in the backward direction with the elastic and inelastic channel separation obtained through FPD-CED coincidences. The shapes of the Focal Plane Detectors follow contours of equal Q^2 bins calculated from the kinematics of the forward measurement of elastically scattered protons, and the shapes of the Cryostat Exit Window Detectors, an example of which is shown in Fig. 13, are calculated to match the Focal Plane Detector shapes, The Cryostat Exit Detectors will be positioned on the G0 spectrometer exit windows, corresponding to the beam axis coordinate of $\sim$ 180 cm.

The shape of the light guides, also shown schematically in Fig. 13, is driven by space constraints in the detector system. Only the space between each of the 8 G0 sectors is available to collect the light from each scintillator, and guide it to photomultiplier tubes positioned outside the magnetic field of the spectrometer, and out of the path of the electrons scattered from the LH_2 target into the G0 focal plane. Tests are currently under way to determine the light collection efficiency for this detector shape, and this light guide configuration, and preliminary measurements indicate that light collection will not be a problem.

The support structure for both Focal Plane and Cryostat Exit detectors, along with appropriate shielding, is currently being designed at TJNAF, with issues of space constraints and mechanical support taken into account. In addition, the design is such that the CED support will be modular, allowing them to be added to the system after the spectrometer has been rotated for the backward angle measurements.

Special attention in the design of the detector system has also been put into:

- keeping the counting rate in each detector segment $\sim$ 1 MHz or less
- keeping the time-of-flight resolution $\sim$ 1 ns or better
- having good Q^2 resolution

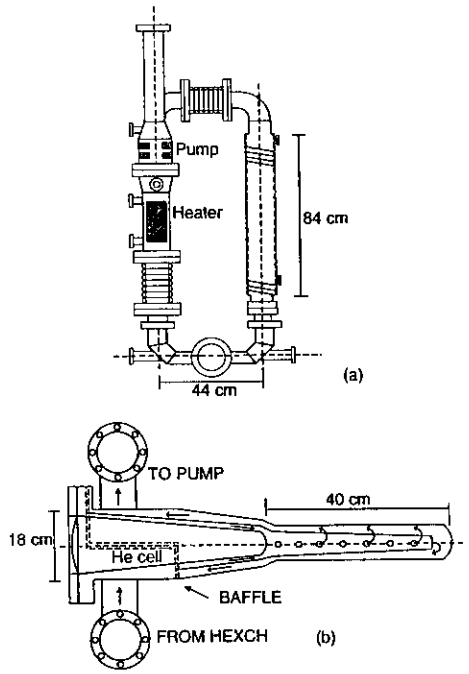

Figure 14: Schematic of SAMPLE target cell.

- keeping the photomultiplier tubes outside of the magnetic field
- keeping the total number of channels reasonably low, reducing the cost
- keeping the thickness of the scintillators low, therefore reducing the neutron background

Finally, the luminosity is achieved by rastering $40\mu A$ average beam current over the G0 liquid hydrogen target. The target used for the SAMPLE experiment at Bates Linear Accelerator Center [52], a schematic of which is shown in Fig. 14, was tested under similar conditions for more than a thousand hours with very satisfactory results, and a modified version of this target will be used for these measurements.

Overall performances of the experimental setup were studied using a GEANT based simulation. Fig. 15 shows the setup as used in the GEANT simulation, as well as a view of the tracks of backward scattered electrons in the elastic and inelastic channels, clearly showing how different CED-FPD coincidences can be used to separate these two channels.

10 Data Acquisition Electronics

Because in the G0 experiment the method for extracting elastic scattering events is significantly different for the forward and backward angle modes of running, a small part of the electronics required will be different. In fact, most of the electronics used for the forward angle measurements will be utilized in a different way for the backward angle measurements.

In the G0 forward angle proton measurements, time of flight spectra will be accumulated in high speed scalers in several time bins for each FPD. In this case, good time of flight resolution

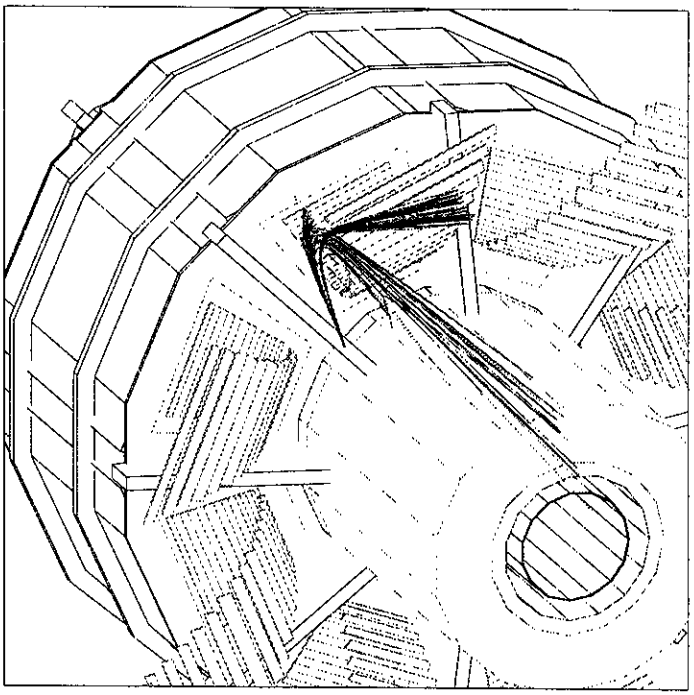

Figure 15: Schematic of setup as used in GEANT simulation, including tracks of both elastically (upper tracks) and inelastically (lower tracks) scattered electrons passing through different combinations of FPD-CED coincidences.

($\sim$ 1 ns) is required to isolate the elastically scattered protons in a given FPD from background. To achieve this, a specialized circuit board will be used to bin each of the focal plane scintillator signals into 1 ns time bins for input to high speed scalers [47]. In this way, the time range of interest (corresponding to the time of flight for elastically scattered protons) between beam pulses delivered to the experiment can be fully sampled, with elastic events well discriminated from background events. It is expected that 12 time bins for each focal plane detector will be sufficient to fully sample this time range, requiring 12 scaler channels to be read for each focal plane detector. In addition, a set of "backing" detectors will be placed behind the focal plane detectors. A coincidence between the backing detectors and the focal plane detectors ensures that a charged particle passed through the focal plane detectors, and can therefore reduce contamination from neutral particle background.

In the backward angle mode of running, it is the electrons which are detected. In this case, the inelastic and elastic channels cannot be separated by time of flight information. The required separation must come from the CED's used in coincidence with the FPD's, which provide measurements of both the scattered electron momentum and angle. In addition, this coincidence ensures that a charged particle was scattered from the target, eliminating the need for the backing detectors used for the forward measurements. All of the photomultiplier tubes and associated power supplies used for the forward angle backing detectors can therefore be used for the CED's during the backward angle measurements. In addition, with the use of 12 CED's for each of the 8 G0 sectors, the existing 12 scaler channels used for the forward angle time bin measurements for each FPD can now be used to count the number of coincidences between every combination of CED and FPD. Because the same number of words will be read in this case as in the forward angle case, there will be no extra demands on the data acquisition system, as well as no additional cost for photomultiplier tubes, associated power supplies, and high speed scalers.

While both the FPD's and CED's will still require constant fraction discrimination and mean-timing to eliminate electronic walk and light propagation time effects within each scintillator during the backward angle measurements, these discriminated signals will then be used as input to logic circuitry, in the form of Programmable Array Logic, presently being designed at Louisiana Tech, to determine which CED's formed coincidences with which FPD's, as shown schematically in Fig. 16. These coincident signals will then be sent directly into their corresponding scaler channels to be read out during the beam helicity change (as discussed in Ref. [47]). Due to the large number of coincidences involved, this logic circuitry will be custom made for this purpose at Louisiana Tech University for significantly less cost than commercially available electronics, and with smaller propagation delay times.

To equip both signals from each CED with constant fraction discriminators, and a mean-timed signal from each CED, 192 CFD and 96 mean-timer channels will be used for the CED's during the backward angle mode of running. Also, as discussed in the G0 Technical Design Report [47], a parallel, monitoring acquisition system will also be implemented to monitor possible drifts in photomultiplier tube gains, and verify the general integrity of the signals used for the parity violation measurements. For these slower time scale measurements, two passive splitters, two ADC channels and one TDC channel will be used for each CED.

11 Summary and Requested Beam Time and Support

We are requesting no additional beam time for these measurements, but rather for the parity violating $N \rightarrow \Delta$ measurements to be recognized as an officially approved TJNAF experiment. The measurements described throughout this proposal will be made during the same running period as the G0 experiment in the backward angle mode. In addition, all beam, hardware,

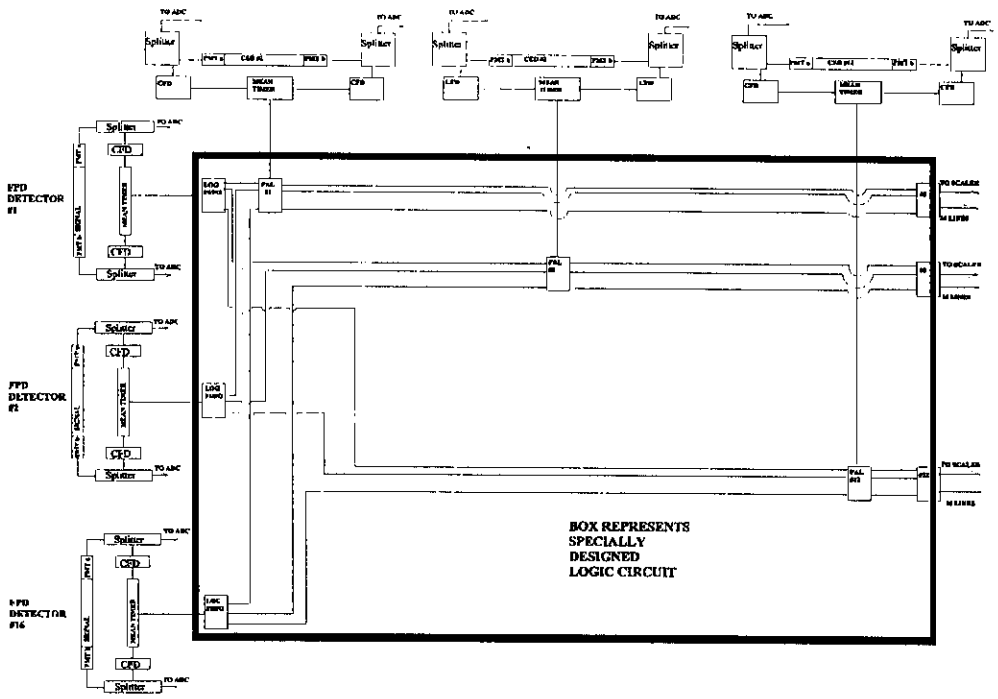

Figure 16: Schematic view of backward angle mode electronics.

and electronics requirements for the G0 backward angle elastic measurements are sufficient to complete the inelastic measurements. Coincidences between the Focal Plane and Cryostat Exit Detectors discussed throughout this proposal are necessary to separate the elastic and threshold inelastic channels during the G0 backward angle measurements, and allow the parity violating asymmetry to be mapped out across the Δ resonance simultaneously. These measurements provide direct access to the axial transition form factor $G^A_{N\Delta}$, the Q^2 dependence of which we will be able to map out in the range $0.05 \leq Q^2 \leq 0.8$ (GeV/c)^2, and represent the first determination of this form factor in the neutral current sector of the weak interaction.

A Details of the Asymmetry

In this appendix, we relate the notation used here to notations used by other authors [24, 8], and show the explicit kinematic dependences of the coefficients of the electromagnetic and weak transition form factors.

In the notation of Ref. [8], the asymmetry, containing only resonant terms, is written

$$A_{RL} = -\frac{2Q^2}{e^2(Q^2+M_Z^2)}\{\alpha g_{A,e} + \beta g_{V,e}\frac{2(E+E')}{M}\frac{W_3 \sin^2\frac{\theta_e}{2}}{2W_1^{EM}\sin^2\frac{\theta_e}{2} + W_2^{EM}\cos^2\frac{\theta_e}{2}}\}, \qquad (15)$$

where $g_{V,e}$ and $g_{A,e}$, are given, in the minimal SU(2)$_L$×U(1) model, by [8]

$$g_{V,e} = \frac{-e}{4\sin\theta_W\cos\theta_W}(1-4\sin^2\theta_W)$$

and

$$g_{A,e} = \frac{e}{4\sin\theta_W\cos\theta_W},$$

where e is the electron charge, and $\sin^2\theta_W$ is the weak mixing angle, α and β are given by [8]

$$\alpha = \frac{e}{2\sin\theta_W\cos\theta_W}(1-2\sin^2\theta_W),$$

$$\beta = -\frac{e}{2\sin\theta_w\cos\theta_W},$$

the structure functions are given by [8]

$$\begin{aligned}
W_1^{EM} &= \frac{c}{6M^4}\{a^2[D_3(Q^2)]^2 + b^2[D_4(Q^2)]^2 + abD_3(Q^2)D_4(Q^2)\},\\
W_2^{EM} &= \frac{2Q^2}{3M^2}\{a[D_3(Q^2)]^2 + c[D_4(Q^2)]^2 + bD_3(Q^2)D_4(Q^2)\},\\
W_3 &= \frac{1}{3M^2}[2aD_3(Q^2)+bD_4(Q^2)]\{(b-2c)\frac{M}{2M'}C_3^A(Q^2)+\frac{b}{2}C_4^A(Q^2)-M^2C_5^A(Q^2)\},
\end{aligned} \tag{16}$$

with

$$\begin{aligned}
a &= (M+M')^2+Q^2,\\
b &= (M+M')(M-M')+Q^2,\\
c &= (M-M')^2+Q^2,
\end{aligned} \tag{17}$$

and

$$\begin{aligned}
D_3(Q^2) &= -\frac{M}{M'}C_3^\gamma(Q^2),\\
D_4(Q^2) &= \frac{M}{M'}C_3^\gamma(Q^2)+C_4^\gamma(Q^2).
\end{aligned} \tag{18}$$

To convert coupling strengths, consider only the first term, and assume $Q^2 \ll M_Z^2$. Then,

$$\begin{aligned}
A_{RL} &= -\frac{2Q^2}{e^2M_Z^2}\alpha g_{A,e}\\
&= -\frac{2Q^2}{e^2M_Z^2}(\frac{e}{2\sin\theta_W\cos\theta_W})(\frac{e}{4\sin\theta_W\cos\theta_W})(1-2\sin^2\theta_W)\\
&= \frac{2Q^2}{M_Z^2}\frac{1}{8\sin^2\theta_W\cos^2\theta_W}[-(1-2\sin^2\theta_W)].
\end{aligned}$$

Now, we use [24]

$$M_W^2 = M_Z^2\cos^2\theta_W,$$

to get

$$A_{RL} = \frac{2Q^2}{8M_W^2\sin^2\theta_W}[-(1-2\sin^2\theta_W)].$$

Next, we use [24]

$$\frac{G_F}{\sqrt{2}} = \frac{g^2}{8M_W^2}$$

and

$$e = g \sin\theta_W$$

to obtain

$$A_{RL} = \frac{2Q^2}{e^2}\frac{G_F}{\sqrt{2}}[-(1-2\sin^2\theta_W)].$$

Finally, we use

$$e^2 = 4\pi\alpha$$

to get

$$\begin{aligned} A_{RL} &= \frac{G_F}{\sqrt{2}}\frac{Q^2}{2\pi\alpha}[-(1-2\sin^2\theta_W)] \\ &= \frac{G_F}{\sqrt{2}}\frac{Q^2}{2\pi\alpha}\tilde{\alpha}. \end{aligned}$$

Similarly,

$$-\frac{2Q^2}{e^2 M_Z^2}\beta g_{V,e} = \frac{G_F}{\sqrt{2}}\frac{Q^2}{2\pi\alpha}\tilde{\beta}.$$

We now have

$$A_{RL} = \frac{G_F}{\sqrt{2}}\frac{Q^2}{2\pi\alpha}\{\tilde{\alpha} + \tilde{\beta}\frac{(2\tan^2\frac{\theta_e}{2})W_3}{(2\tan^2\frac{\theta_e}{2})W_1^{EM} + W_2^{EM}}\}, \tag{19}$$

where W_1^{EM}, W_2^{EM}, and W_3 are given by Eq. (16) above, and we have divided both numerator and denominator of Eq. (15) by $\cos^2\frac{\theta_e}{2}$ (we note that no measurements will be made at θ_e=180°). Carrying through some algebra yields

$$\begin{aligned} (2\tan^2\frac{\theta_e}{2})W_1^{EM} + W_2^{EM} = \; & h_{33}(Q^2,\theta_e)[C_3^\gamma(Q^2)]^2 + h_{34}(Q^2,\theta_e)C_3^\gamma(Q^2)C_4^\gamma(Q^2) \\ & + h_{44}(Q^2,\theta_e)[C_4^\gamma(Q^2)]^2, \end{aligned} \tag{20}$$

where

$$\begin{aligned} h_{33}(Q^2,\theta_e) &= \frac{1}{3M'^2}[(a^2+b^2-ab)c\frac{\tan^2\frac{\theta_e}{2}}{M^2} + 2(a+c-b)Q^2], \\ h_{34}(Q^2,\theta_e) &= \frac{1}{3MM'}[(2b^2-ab)c\frac{\tan^2\frac{\theta_e}{2}}{M^2} + 2(2c-b)Q^2], \\ h_{44}(Q^2,\theta_e) &= \frac{1}{3M^2}[b^2c\frac{\tan^2\frac{\theta_e}{2}}{M^2} + 2cQ^2], \end{aligned} \tag{21}$$

with a, b, and c defined in Eq. (17).

Similarly,

$$\begin{aligned} (2\tan^2\frac{\theta_e}{2})W_3 = \; & [h_3(Q^2,\theta_e)C_3^\gamma(Q^2) + h_4(Q^2,\theta_e)C_4^\gamma(Q^2)] \times \\ & [g_3(Q^2)C_3^A(Q^2) + g_4(Q^2)C_4^A(Q^2) + g_5(Q^2)C_5^A(Q^2)], \end{aligned} \tag{22}$$

where

$$
\begin{aligned}
h_3(Q^2,\theta_e) &= \frac{2M}{3M'}(b-2a)\frac{\tan^2\frac{\theta_e}{2}}{M^2}, \\
h_4(Q^2,\theta_e) &= \frac{2}{3}b\frac{\tan^2\frac{\theta_e}{2}}{M^2}, \\
g_3(Q^2) &= \frac{M}{2M'}(b-2c), \\
g_4(Q^2) &= \frac{b}{2}, \\
g_5(Q^2) &= -M^2.
\end{aligned}
\tag{23}
$$

Substituting Eq.'s (20) and (22) into Eq. (19) yields

$$
A_{RL} = \frac{G_F}{\sqrt{2}}\frac{Q^2}{2\pi\alpha}[\tilde{\alpha}+\tilde{\beta}F(Q^2,E,E',\theta_e)], \tag{24}
$$

where

$$
F(Q^2,E,E',\theta_e) = \frac{(E+E')}{M}H^{EM}(Q^2,\theta_e)G^A_{N\Delta}(Q^2), \tag{25}
$$

with

$$
H^{EM}(Q^2,\theta_e) = \frac{h_3(Q^2,\theta_e)C_3^\gamma(Q^2)+h_4(Q^2,\theta_e)C_4^\gamma(Q^2)}{h_{33}(Q^2,\theta_e)[C_3^\gamma(Q^2)]^2+h_{34}(Q^2,\theta_e)C_3^\gamma(Q^2)C_4^\gamma(Q^2)+h_{44}(Q^2,\theta_e)[C_4^\gamma(Q^2)]^2}, \tag{26}
$$

and

$$
G^A_{N\Delta}(Q^2) = g_3(Q^2)C_3^A(Q^2)+g_4(Q^2)C_4^A(Q^2)+g_5(Q^2)C_5^A(Q^2). \tag{27}
$$

We note here that, in full generality, $C_6^A(Q^2)$ would contribute (see Eq. (3)), but enters into this part of the asymmetry with a factor of $\frac{m_e}{M}$ and is therefore neglected [8]. Additionally, the form of $H^{EM}(Q^2,\theta_i)$ depends on the assumption that $C_5^\gamma(Q^2)=0$. The physics justification for this assumption is two-fold: a) the theory of the spin-$\frac{3}{2}$ field requires that $C_4^\gamma(Q^2)=C_5^\gamma(Q^2)=0$, and b) the single pion photoproduction and electroproduction data can be adequately described with $C_4^\gamma(Q^2)=C_5^\gamma(Q^2)=0$, or $C_5^\gamma(Q^2)=0$ and $C_4^\gamma(Q^2)=-\frac{M}{M+M'}C_3^\gamma(Q^2)$ [8].

B Discussion of Non-Resonant Background

As discussed throughout this proposal, the yield for 1 pion electroproduction from the proton is dominated by the $N\rightarrow\Delta$ resonance, but there are non-resonant processes which contribute. While estimates have been given as to the contribution these processes make to the parity violating asymmetry, the non-resonant background must be understood for a proper interpretation of the data to be obtained from these proposed measurements. To bring out the main features of the parity violating asymmetry in inclusive π electroproduction in the Δ resonance region, an analysis of the asymmetry obtained from the incoherent summation of the coincident $p\pi^0$ and $n\pi^+$ charge states (*i.e.*, the decay of the Δ^+) has been performed [9]. They find

$$
A^\pi_{RL} = -\frac{1}{2}\frac{G_F}{\sqrt{2}}\frac{Q^2}{2\pi\alpha}(\Delta^\pi_{(1)}+\Delta^\pi_{(2)}+\Delta^\pi_{(3)}), \tag{28}
$$

where $\Delta^\pi_{(1)}$ corresponds to the axial vector electron-vector quark isovector resonant contribution, $\Delta^\pi_{(2)}$ gives the axial vector electron-vector quark non-resonant background contributions (both isovector and isoscalar), and $\Delta^\pi_{(3)}$ gives the vector electron-axial vector quark contribution (both resonant isovector and non-resonant isoscalar). These terms are given explicitly by

$$
\begin{aligned}
\Delta^{\pi}_{(1)} &= g^e_A \xi^{T=1}_V \\
F^2\Delta^{\pi}_{(2)} &= -2g^e_A\xi^n_V \sum_l \Re \\
&\times \{v_T[l(l+1)^2(\frac{3}{\sqrt{2}}M^{0*}_{l+}M^{\frac{1}{2}}_{l+} - 3|M^0_{l+}|^2) + l^2(l+1)(\frac{3}{\sqrt{2}}M^{0*}_{l-}M^{\frac{1}{2}}_{l-} - 3|M^0_{l-}|^2) \\
&+ (l+2)(l+1)^2(\frac{3}{\sqrt{2}}E^{0*}_{l+}E^{\frac{1}{2}}_{l+} - 3|E^0_{l+}|^2) + l^2(l-1)(\frac{3}{\sqrt{2}}E^{0*}_{l-}E^{\frac{1}{2}}_{l-} - 3|E^0_{l-}|^2)] \\
&+ v_L[(l+1)^3\frac{3}{\sqrt{2}}S^{0*}_{l+}S^{\frac{1}{2}}_{l+} - 3|S^0_{l+}|^2) + l^3(\frac{3}{\sqrt{2}}S^{0*}_{l-}S^{\frac{1}{2}}_{l-} - 3|S^0_{l-}|^2)]\} \qquad (29) \\
F^2\Delta^{\pi}_{(3)} &= 2g^e_V v_{T'} \sum_l \Re\{l(l+1)^2\tilde{E}^{5*}_{l+}M_{l+} - (l+1)^2(l+2)\tilde{M}^{5*}_{l+}E_{l+} \\
&- l^2(l+1)\tilde{E}^{5*}_{l-}M_{l-} + l^2(l-1)\tilde{M}^{5*}_{l-}E_{l-}\},
\end{aligned}
$$

where the E's, M's, and S's are transverse electric, transverse magnetic, and longitudinal multipoles, respectively [25, 53, 54], their subscripts denote the angular momentum and parity, their superscripts indicate the isospin decomposition,

$$
\begin{aligned}
v_T &= \frac{1}{2}|\frac{Q^2}{q^2}| + \tan^2\frac{\theta_e}{2} \\
v'_T &= \tan\frac{\theta_e}{2}\sqrt{|\frac{Q^2}{q^2}| + \tan^2\frac{\theta_e}{2}} \qquad (30) \\
v_L &= |\frac{Q^2}{q^2}|^2,
\end{aligned}
$$

and F^2 corresponds to the inclusive electromagnetic cross section, normalized to the Mott cross section (in the notation used here, F^2 corresponds to $2W_1^{EM}\sin^2\frac{\theta_e}{2} + W_2^{EM}\cos^2\frac{\theta_e}{2}$). The conversion of coupling constants has been given in Ref. [9], where they find

$$
\begin{aligned}
g^e_A\xi^{T=1}_V &= -2\tilde{\alpha}, \\
-2g^e_A\xi^n_V &= -2(\tilde{\alpha} - 3\tilde{\gamma}).
\end{aligned}
$$

Also, we note that the axial contribution, $F^2\Delta^{\pi}_{(3)}$, has no isospin decomposition given here. The contributions to this term, however, come from three sources [31]: the dominant isovector piece, which includes the axial transition form factor $G^A_{N\Delta}(Q^2)$; the primordial weak isoscalar axial current, which vanishes in the minimal $SU(2)_L\times U(1)$ standard model (and becomes nonvanishing only when weak radiative corrections are included); and the heavy quark isoscalar axial currents, which were originally neglected in writing down the phenomenological Lagrangian for electron nucleon scattering (denoted by dots in Eq. (5)), and are expected to be only a few percent of the isovector contribution [31]. Thus, for a first generation inelastic channel parity violation measurement, the axial term may be taken to have a contribution only from the isovector piece containing the axial transition form factor $G^A_{N\Delta}(Q^2)$. Thus, we may write

$$
A^{\pi}_{RL} = \frac{G_F}{\sqrt{2}}\frac{Q^2}{q\pi\alpha}[\tilde{\alpha} + (\tilde{\alpha} - 3\tilde{\gamma})\Delta^{\pi'}_{(2)} + \tilde{\beta}F(Q^2, E, E', \theta_e)], \qquad (31)
$$

where $F(Q^2, E, E', \theta_e)$ is given by Eq. (7) and in Appendix A, and

$$
\Delta^{\pi'}_{(2)} = \frac{\Delta^{\pi}_{(2)}}{-2(\tilde{\alpha} - 3\tilde{\gamma})}. \qquad (32)
$$

As can be seen from Eq. (29), there are an infinite number of multipoles which comprise the non-resonant background contribution to the 1 pion electroproduction asymmetry, with both isovector and isoscalar pieces. Thus, even in keeping only the leading order multipoles implies that an isospin decomposition is necessary to describe the non-resonant contribution. As discussed earlier, an extensive data base for photoproduction from both the proton and neutron [32, 33, 34, 35, 36, 37] exist, and complete multipole and isospin decompositions have been done at the photon point [55, 38]. Such a decomposition does not exist for finite Q^2, as electroproduction data on neutron targets is quite limited. Once these data exist [40], a more thorough description of the background will be possible.

In addition, this analysis [9] was performed on the incoherent summation of final charge states, where no interference between resonant and non-resonant multipoles contributes. The parity violating asymmetry from inclusive 1 pion electroproduction will certainly have contributions from these interferences, and must be taken into account for a description of these measurements. Again, an estimate of the contributions from both the background and the interferences can be made with the use of a model [13], throughout the entire 1 pion production region. Near the resonance, both of these contributions are expected to be small (see Fig. 2), and contribute with opposite signs, resulting in the resonant contribution dominating the asymmetry. As one moves away from the resonance, the relative sizes of these contributions is expected to change, as can be seen in Fig. 17, where we plot the individual contributions to the asymmetry as a function of photon equivalent energy k_γ, where

$$k_\gamma = \frac{(E - E')}{2} + \frac{Q^2}{2M}, \tag{33}$$

for two different values of Q^2, along with an estimate of our expected statistical precision to be achieved at each Q^2 value studied in Ref. [13]. At low Q^2, and near threshold, the non-resonant background makes a large contribution, but decreases in strength with increasing excitation energy, while the resonant contribution increases. In the context of this phenomenological model, there is a curious cancellation of non-resonant and interference terms as the excitation energy increases, which persists as a function of Q^2, resulting in a parity violating asymmetry which has very little dependence on excitation energy.

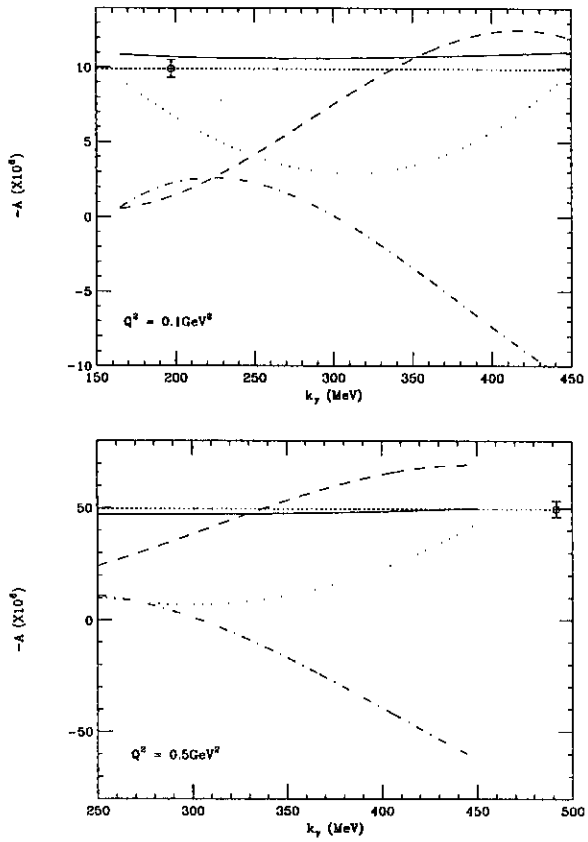

Figure 17: Asymmetries as a function of photon equivalent energy, k_γ, for Q^2=0.1 (GeV/c)^2 (upper) and Q^2=0.5 (GeV/c)^2 (lower), including expected statistical precision for each Q^2 value. The meaning of the curves is the same as in Fig. 2.

References

[1] D. H. Beck, CEBAF experiment E91-017.

[2] D.B. Kaplan and A. Manohar, Nucl. Phys. **B310**, 527 (1988).

[3] R.D. McKeown, Phys. Lett. B **219**, 140(1989).

[4] D.H. Beck, Phys. Rev. D **39**, 3248 (1989).

[5] B.A. Mueller *et al.*, Phys. Rev. Lett. **78**, 3824 (1997), and references therein.

[6] R.N. Cahn and F.J. Gilman, Phys. Rev. D **17**, 1313 (1978)

[7] D.R.T. Jones and S.T. Petcov, Phys. Lett. B **91**, 137 (1980).

[8] L.M. Nath, K. Schilcher, and M. Kretzschmar, Phys. Rev. D **25**, 2300, 1982.

[9] M.J. Musolf, T.W. Donnelly, J. Dubach, S.J. Pollock, S. Kowalski, and E.J. Beise, Phys. Rep. **239**, 1 (1994).

[10] M. Bourdeau and Nimai C. Mukhopadhyay, Phys. Rev. Lett. **58**, 976 (1987)

[11] T.R. Hemmert, B.R. Holstein, and Nimai C. Mukhopadhyay, Phys. Rev. D **51**, 158 (1995).

[12] J. Liu, Nimai C. Mukhopadhyay, and L. Zhang, Phys. Rev. C **52**, 1630 (1995).

[13] H.-W. Hammer and D. Drechsel, Z. Phys. **A353**, 321 (1995).

[14] L. Elouadrhiri, CEBAF Experiment E94-005.

[15] K. Bätzner *et al.,* Phys. Lett. B **39**, 575 (1972).

[16] S. Nozawa and T.-S.H. Lee, Nucl. Phys. A **513**, 511 (1990).

[17] V. Burkert and R. Minehart CEBAF E89-037.

[18] J. Napolitano and P. Stoler CEBAF E94-014.

[19] S.L. Glashow, Nucl. Phys. **22**, 579 (1961).

[20] A. Salam and J.C. Ward, Phys. Lett. **13**, 168 (1964).

[21] C.J. Bebek *et al.,* Phys. Rev. D **15**, 594 (1977).

[22] W. Rarita and J. Schwinger, Phys. Rev. **60**, 61 (1941).

[23] C.H. Llewellyn Smith, Phys. Rep. **3**, 261 (1972).

[24] P.Q. Hung and J.J. Sakurai, Ann. Rev. Nucl. Part. Sci. **31**, 375 (1981).

[25] S.L. Adler, Ann. Phys. **50**, 189 (1968).

[26] S.J. Barish *et al.,* Phys. Rev. D **19**, 2521 (1979).

[27] T. Kitagaki *et al.,* Phys. Rev. D **42**, 1331 (1990).

[28] P. Joos *et al.,* Phys. Lett. B **62**, 230 (1976).

[29] S. Choi *et al.,* Phys. Rev. Lett. **71**, 3927 (1993).

[30] S.L. Adler and W.I. Weisberger, Phys. Rev. **169**, 1392 (1968).

[31] T.W. Donnelly, private communication.

[32] W. Pfeil and D. Schwela, Nucl. Phys. B **45**, 379 (1971).

[33] F.A. Berends and A. Donnachie, Nucl. Phys. B **84**, 342 (1975).

[34] S. Suzuki, S. Kurokawa, and K. Kondo, Nucl. Phys. B **68**, 413 (1974).

[35] I.I. Miroshnichenko *et al.,* Sov. J. Nucl. Phys. **32**, 339 (1980).

[36] V.A. Get'man *et al.,* Sov. J. Nucl. Phys. **38**, 230 (1983).

[37] V.F. Grushin *et al.,* Sov. J. Nucl. Phys. **38**, 881 (1983).

[38] R.M. Davidson and Nimai C. Mukhopadhyay, Phys. Rev. D **42**, 20 (1990).

[39] R.M. Davidson, Nimai C. Mukhopadhyay, and R. Wittman, Phys. Rev. Lett. **56**, 804 (1986).

[40] V. Burkert in N^* *WORKSHOP* - "Partial Wave Analysis," CEBAF, Nov. 9-12, 1995.

[41] Sai-Ping Li, E.M. Henley, and W-Y.P. Hwang, Ann. of Phys. **143**, 372 (1982).

[42] J. W. Lightbody and J. S. O'Connel, Computers in Physics **2**, 57 (1988).

[43] F. W. Brasse *et al.*, Nucl. Phys. B **110**, 413 (1976).

[44] F. W. Brasse *et al.*, NC **55A**, 679 (1967).

[45] F. James and M. Roos, CERN computer center program, (1977).

[46] R. Laszewski, private communication.

[47] G0 Technical Design Report, Nuclear Physics Laboratory, University of Illinois at Urbana-Champaign, 1993.

[48] B. Rossi and K. Greisen, Rev. Mod. Phys. **13**, 240 (1941).

[49] S.M. Seltzer and M.J. Berger, Nucl. Instr. and Meth. B **12**, 95 (1985).

[50] GEANT Detector Description and Simulation Tool, *CERN Program Library Long Writeup W5013*, CERN, Geneva, 1993

[51] N. Simicevic and S.P. Wells, LaTech Technical Report, CAPS-97-09a.

[52] E.J. Beise *et al.*, Nucl. Instr. Meth. A **378**, 383 (1996).

[53] S.J. Pollock, Ph.D. Thesis, Stanford University (1987) unpublished.

[54] A.S. Raskin and T.W. Donnelly, Ann. Phys. **191**, 78 (1989).

[55] W.J. Metcalf and R.L. Walker, Nucl. Phys. B **76**, 253 (1974).